

# Supramolecular Polymer-Based Nanomedicine: High Therapeutic Performance and Negligible Long-Term Immunotoxicity

Guocan Yu,<sup>†</sup> Xinlian Zhao,<sup>‡</sup> Jiong Zhou,<sup>§</sup> Zhengwei Mao,<sup>\*,‡</sup> Xiaolin Huang,<sup>†</sup> Zhantong Wang,<sup>†</sup> Bin Hua,<sup>§</sup> Yijing Liu,<sup>†</sup> Fuwu Zhang,<sup>†</sup> Zhimei He,<sup>†</sup> Orit Jacobson,<sup>†</sup> Changyou Gao,<sup>‡</sup> Weilin Wang,<sup>‡</sup> Chunyang Yu,<sup>\*,||</sup> Xinyuan Zhu,<sup>||</sup> Feihe Huang,<sup>\*,§</sup> and Xiaoyuan Chen<sup>\*,†||</sup>

<sup>†</sup>Laboratory of Molecular Imaging and Nanomedicine, National Institute of Biomedical Imaging and Bioengineering, National Institutes of Health, Bethesda, Maryland 20892, United States

<sup>‡</sup>MOE Key Laboratory of Macromolecular Synthesis and Functionalization, Department of Polymer Science and Engineering, and

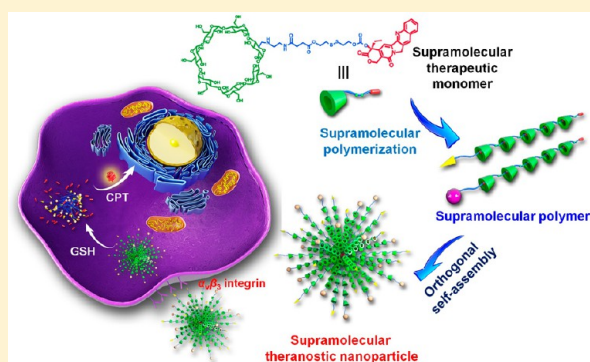
<sup>§</sup>State Key Laboratory of Chemical Engineering, Center for Chemistry of High-Performance & Novel Materials, Department of Chemistry, Zhejiang University, Hangzhou 310027, People's Republic of China

<sup>||</sup>School of Chemistry and Chemical Engineering, State Key Laboratory of Metal Matrix Composites, Shanghai Jiao Tong University, 800 Dongchuan Road, Shanghai 200240, China

<sup>‡</sup>Department of Surgery, First Affiliated Hospital of Zhejiang University, Hangzhou 310027, People's Republic of China

## Supporting Information

**ABSTRACT:** Nanomedicines have achieved several breakthroughs in cancer treatment over the past decades; however, their potential immunotoxicities are ignored, which results in serious adverse effects and greatly reduces the potential in clinical translation. Herein, we innovatively develop a theranostic supramolecular polymer using  $\beta$ -cyclodextrin as the host and camptothecin (CPT) as the guest linked by a glutathione-cleavable disulfide bond. The supramolecular polymerization remarkably increases the solubility of CPT by a factor of 232 and effectively inhibits its lactone ring opening in physiological environment, which is favorable for intravenous formulation and maintenance of the therapeutic efficacy. Supramolecular nanoparticles can be prepared through orthogonal self-assembly driven by  $\pi$ - $\pi$  stacking interaction, host-guest complexation, and hydrogen bonds. The sophisticated nanomedicine constructed from the obtained supramolecular polymer can be specifically delivered to tumor sites and rapidly excreted from body after drug release, thus effectively avoiding systemic toxicity, especially long-term immunotoxicity. In vivo investigations demonstrate this supramolecular nanomedicine possesses superior antitumor performance and antimetastasis capability. This pioneering example integrating the advantages of the dynamic nature of supramolecular chemistry and nanotechnology provides a promising platform for cancer theranostics.



## INTRODUCTION

The past decades have witnessed a vigorous development of nanomedicines for the systemic and controlled delivery of drugs for the treatment of malignancies.<sup>1–6</sup> By fully taking advantage of nanotechnology, nanomedicines overcome several drawbacks of traditional chemotherapeutics, such as (i) increasing the solubility/stability and pharmacokinetics of the drugs in blood, (ii) prevention of nonspecific interactions during circulation, (iii) enhancement of drug accumulation in tumor tissue through enhanced permeability and retention (EPR) effect and active targeting capability, and (iv) reducing the side effect. However, one important prerequisite for these nanoscaled drug carriers that is almost totally ignored is their long-term immunotoxicity.<sup>7–10</sup> Although the synthetic polymers widely utilized in constructing nanomedicines are biodegradable and biocompatible, the degradation always

takes several weeks or even several months because of their high molecular weight and stable covalent connections between the monomers. The poor metabolism and elimination properties of the exogenous nanomaterials always result in the interactions with various components of the immune system, thus inevitably leading to serious adverse reactions and potential immunotoxicity that may terminate the therapy or reduce the anticancer efficacy.<sup>11–13</sup> Therefore, the search for new polymers with the ability to be rapidly and completely degraded into small molecules with responsive linkages in backbone is extremely urgent to effectively avoid recognition by the immune system, overcoming nanomaterials-induced toxicity.

Received: April 25, 2018

Published: June 6, 2018

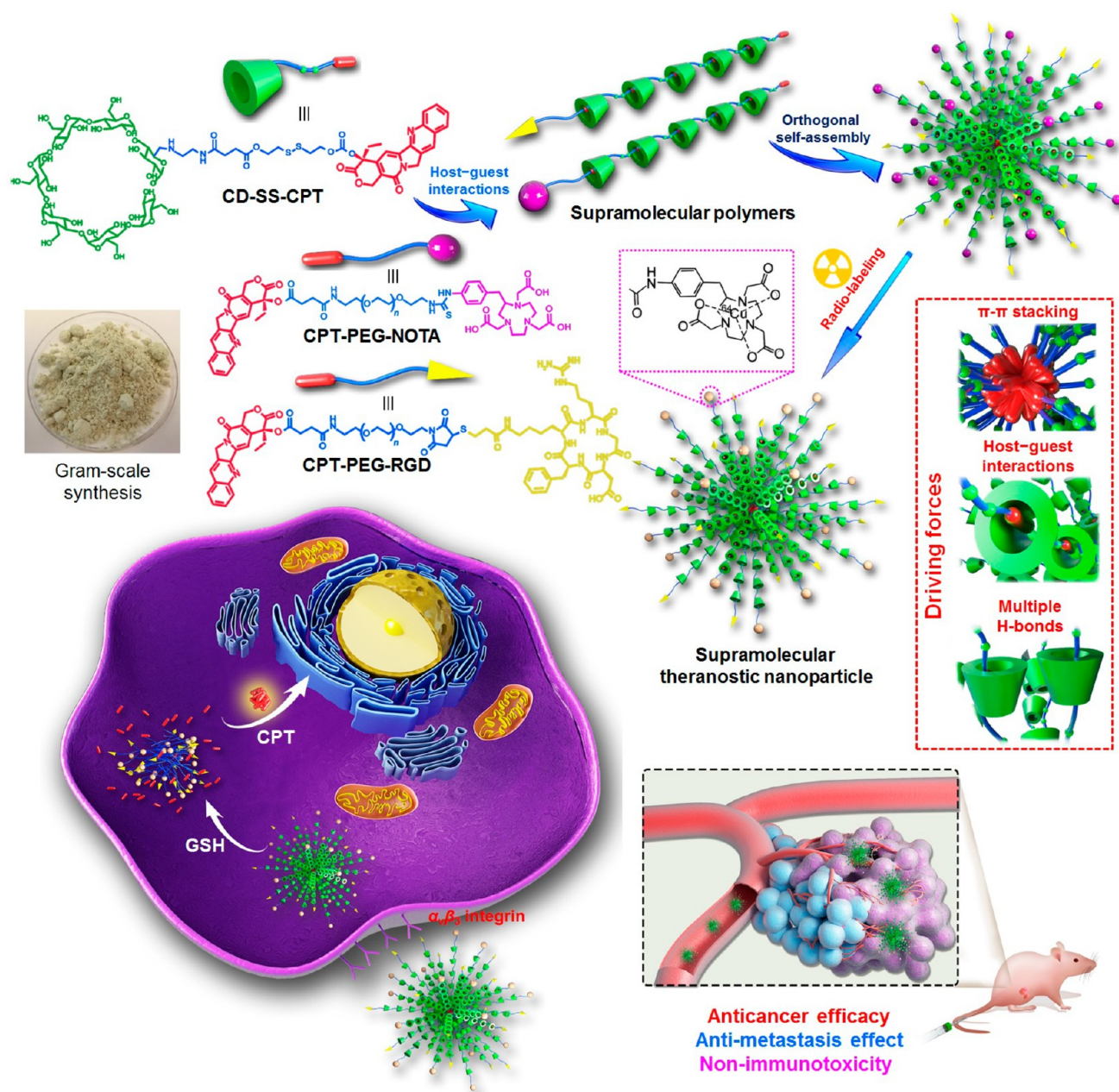


**Figure 1.** Supramolecular polymers constructed from the host–guest complexations between CPT and  $\beta$ -CD orthogonally self-assemble into SNPs, which are stabilized by  $\pi$ - $\pi$  stacking between the CPT in the core, host–guest complexation between CPT and  $\beta$ -CD, and multiple H-bonds between the  $\beta$ -CD. After internalization by the cancer cells, SNPs rapidly dissociated arising from the cleavage of disulfide bond ( $-SS-$ ) by intracellular GSH. These theranostic SNPs possess excellent anticancer efficacy, antimetastasis effect, and negligible long-term immunotoxicity.

In contrast to traditional polymers, the repeating units in the supramolecular polymers (SPs) are connected together by directional and reversible noncovalent interactions, endowing the resultant supramolecular polymeric nanomaterials with abundant stimuli-responsiveness, which opens the prospect of many new applications.<sup>14–18</sup> However, the employment of SPs as therapeutic agents or drug delivery systems is very rare, mainly attributed to the low stability of noncovalent bonds. A majority of noncovalent interactions including H-bonds, metal coordinations, and electrostatic interactions are easily destroyed in physiological environment due to the existence of numerous proteins, metals, and salts. Host–guest complexations based on the hydrophobic interactions are feasible options to fabricate theranostic SPs integrating imaging and

therapeutic functions. Among various macrocyclic hosts, cyclodextrins (CDs) are the most suitable and fascinating hosts for supramolecular polymerizations in aqueous solution because of their excellent biocompatibility and strong binding affinity toward a wide range of guests.<sup>19–23</sup> Although a dozen functional SPs have been prepared already on the basis of the molecular recognition motifs between CDs and hydrophobic guests, rare examples were reported by using anticancer drugs as the guests to construct therapeutic SPs for in vivo cancer theranostics. Moreover, the resultant SPs need to be thoughtfully protected, because the hydrophobic domains in the protein may interfere with the noncovalent linkages, which tend to dissociate the SPs, possibly causing side effects to normal tissues. Because of its poor solubility and easy lactone–

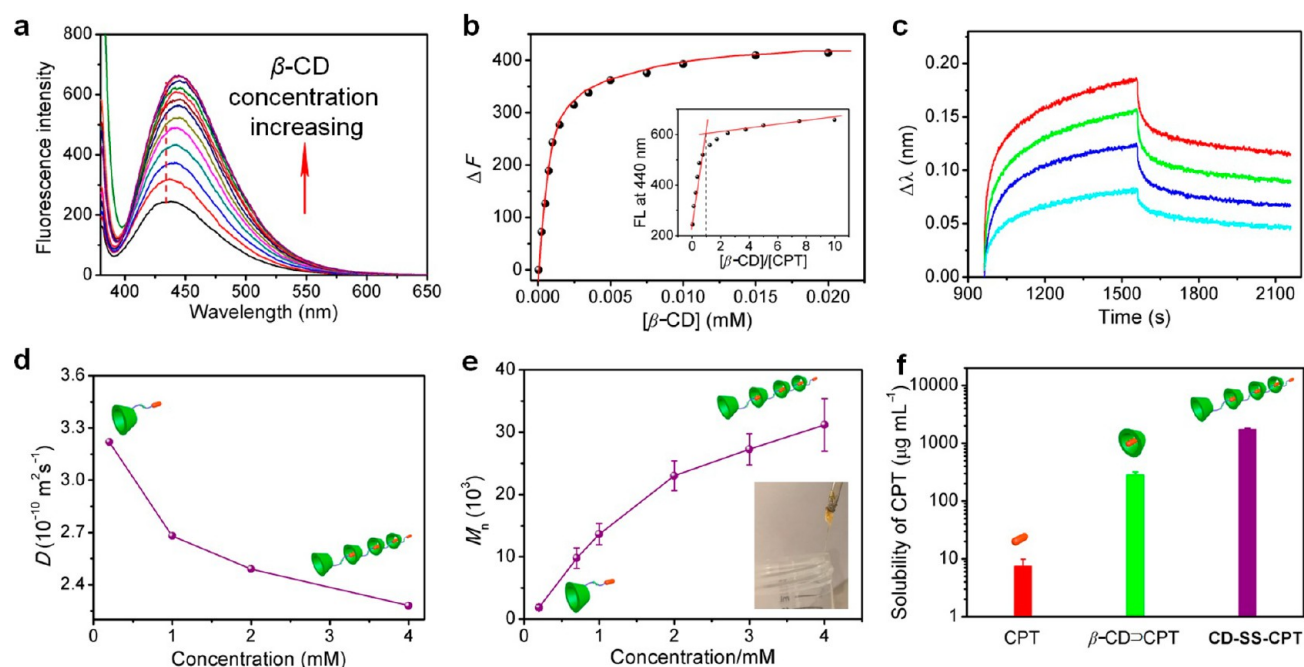


**Figure 2.** (a) Fluorescence spectra of CPT in aqueous solution upon gradual addition of  $\beta$ -CD. (b) The fluorescence intensity changes at 440 nm upon addition of  $\beta$ -CD. The red solid line was obtained from a nonlinear curve-fitting. Inset: Mole ratio plot for CPT and  $\beta$ -CD. (c) Association/dissociation curves of CPT and  $\beta$ -CD in PBS as measured by biolayer interferometry. (d) Concentration-dependent changes in  $D$  values of CD-SS-CPT. (e) Concentration-dependent changes in molecular weight of CD-SS-CPT determined by VPO. Inset: Photographic image of a rod-like fiber drawn from the highly viscous aqueous solution of CD-SS-CPT. (f) Solubility evaluation of CPT for free CPT,  $\beta$ -CD $\supset$ CPT, and CD-SS-CPT. Data are expressed as means  $\pm$  s.d.

carboxylate transformation in blood, the clinical translation of camptothecin (CPT) is greatly limited.<sup>24–27</sup> We foresee that these obstacles can be effectively solved through supramolecular polymerization, because CPT with a suitable size is an ideal building block for the construction of SPs.

Herein, we design and synthesize an AB-type supramolecular monomer (CD-SS-CPT), where the  $\beta$ -cyclodextrin ( $\beta$ -CD) host and CPT guest are linked by a disulfide bond, endowing the supramolecular polymer with glutathione (GSH) responsive capability (Figure 1). Through supramolecular polymerization in water, the solubility of CPT is significantly increased by a factor of 232. On the other hand, the lactone form of CPT is effectively preserved in physiological environment upon formation of inclusion complex, greatly maintaining its anticancer activity. To improve the stability of CD-SS-CPT as well as to introduce targeting and imaging abilities, CPT-PEG-RGD or CPT-PEG-NOTA was introduced to prepare nanoparticles (NPs) through orthogonal self-assembly in aqueous solution, where targeting ligand (cRGDFK) and positron emission tomography (PET) tracer (<sup>64</sup>Cu) can be incorporated into the NPs. The PEG shell outside can be used to avoid protein absorption, which works together with the multiple intermolecular hydrogen bonds between the  $\beta$ -CD and  $\pi$ - $\pi$  stacking interaction between the CPT in the core to stabilize the formed NPs. In vitro and in vivo investigations demonstrate that this supramolecular nanomedicine exhibits excellent anticancer efficacy and antimetastasis effect. More importantly, negligible systemic toxicity and long-term immunotoxicity were detected, benefiting from the advantages of supramolecular chemistry and nanotechnology.

## RESULTS AND DISCUSSION

**Fabrication of Supramolecular Polymer.** The supramolecular monomer (CD-SS-CPT) could be synthesized in gram-scale through several steps in a high yield (>80%) and purity (>98%) without time-consuming purification by column chromatography (Figures S1–5), which was extremely important for potential clinical translation. Other building blocks including CD-CC-CPT, CPT-PEG-NOTA, CPT-PEG-RGD, CD-NOTA, and CPT-Biotin were also successfully synthesized and fully characterized (Figures S6–20). For  $\beta$ -CD, the interior of the cavity is nonpolar and the maximum internal diameter is 7.8 Å,<sup>28</sup> permitting the formation of a stable [2]pseudorotaxane-type inclusion complex with CPT. On the other hand, the modification of  $\beta$ -CD at its C<sub>6</sub> position facilitates CD-SS-CPT to form linear supramolecular polymer, where the CPT tail penetrates into the cavity of  $\beta$ -CD from the large opening. The host–guest interaction between  $\beta$ -CD and CPT was first investigated by fluorescence titration experiment. By the gradual addition of  $\beta$ -CD into the aqueous solution containing CPT, the characteristic emission of CPT increased effectively accompanied by a red shift of the maximum peak (Figure 2a), because the  $\pi$ - $\pi$  stacking interaction between the CPT was greatly inhibited by forming an inclusion complex ( $\beta$ -CD $\supset$ CPT). According to the titrations, the stoichiometry of the host–guest complex was calculated to be 1:1 (Figure 2b). Using a nonlinear curve-fitting method, the association constant was calculated to be  $(1.68 \pm 0.17) \times 10^4 \text{ M}^{-1}$ , which is strong enough to construct SP in aqueous solution (Figure 2b and Figures S21–23). Moreover, biolayer interferometry was utilized to investigate the binding kinetics of  $\beta$ -CD and CPT in PBS using CPT-Biotin as a model compound. As shown in Figure 2c, the dissociation constant of the host–guest complex was calculated

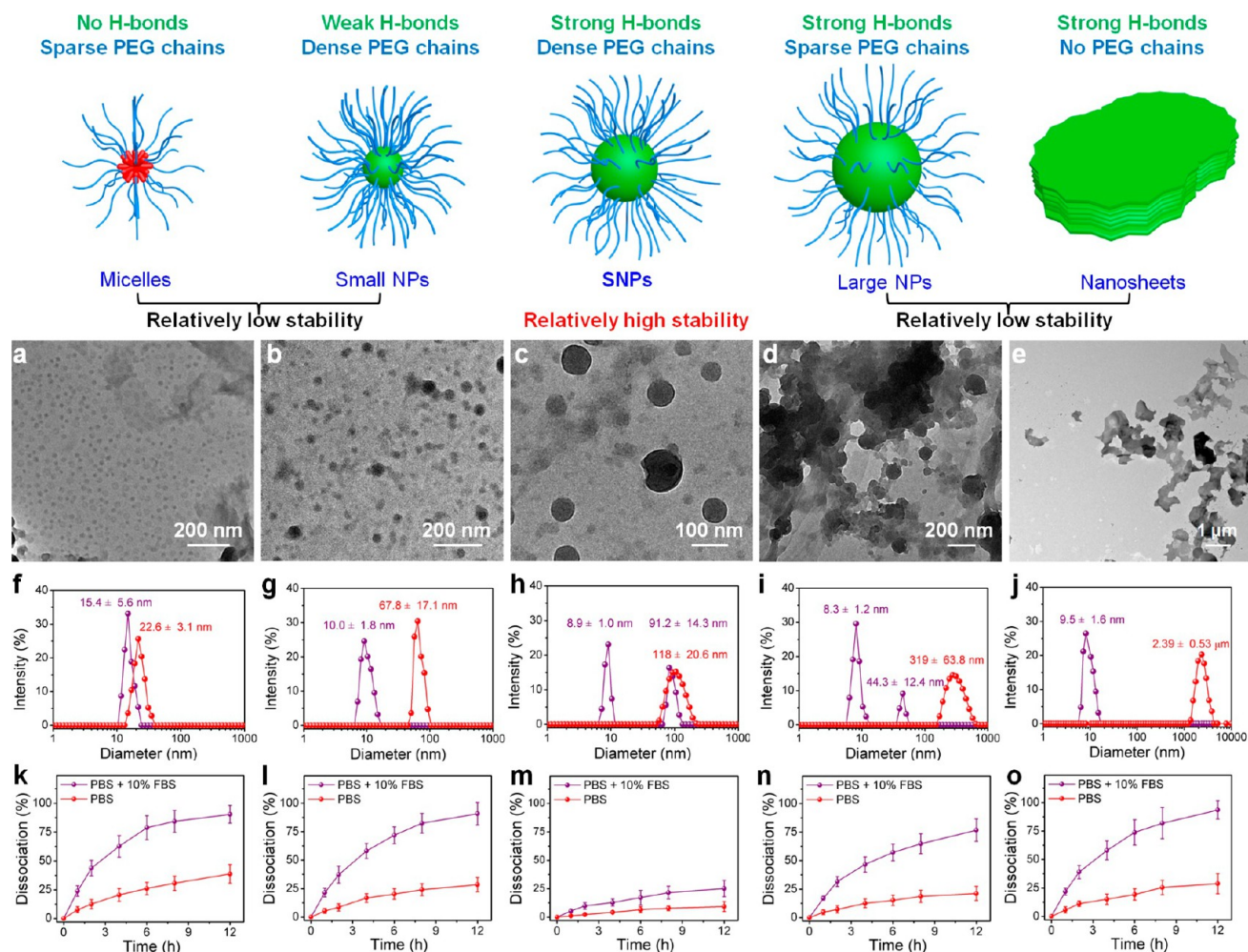


**Figure 3.** TEM images of (a) micelles (CPT-PEG-RGD), (b) small NPs (CD-SS-CPT/CPT-PEG-RGD = 20), (c) SNPs (CD-SS-CPT/CPT-PEG-RGD = 40), (d) large NPs (CD-SS-CPT/CPT-PEG-RGD = 80), and (e) nanosheets (CD-SS-CPT). DLS results of (f) micelle, (g) small NPs, (h) SNPs, (i) large NPs, and (j) nanosheets before (red line) and after (purple line) incubation with 10% FBS for 24 h. Dissociation percentage of (k) micelles, (l) small NPs, (m) SNPs, (n) large NPs, and (o) nanosheets in PBS with (purple line) and without (red line) FBS. Data are expressed as means  $\pm$  s.d.

to be 104  $\mu\text{M}$  from the classic association/dissociation curves, in line with the result obtained from fluorescence titrations. The 2D NOSEY spectrum provided convincing evidence for the formation of inclusion complex (Figure S24). Nuclear Overhauser effect correlations were detected between the signals corresponding to the protons on CPT and  $\beta$ -CD, suggesting that CPT penetrated deeply into the cavity of  $\beta$ -CD driven by hydrophobic interactions.

Various characterizations were employed to confirm the supramolecular polymerization of CD-SS-CPT in aqueous solution. 2D diffusion-ordered NMR spectroscopy (DOSY) investigations indicated that the measured weighted average diffusion coefficients ( $D$ ) considerably decreased from  $3.22 \times 10^{-10}$  to  $2.27 \times 10^{-10} \text{ m}^2 \text{ s}^{-1}$  when the concentration of monomer CD-SS-CPT increased from 0.20 to 4.00 mM (Figure 2d), verifying the concentration-dependent supramolecular polymerization of CD-SS-CPT.<sup>29,30</sup> Vapor pressure osmometry (VPO) measurements demonstrated that the molecular weight increased from 2.09 to 31.2 K as the concentration of CD-SS-CPT increased from 0.20 to 4.00 mM (Figure 2e), indicating that CD-SS-CPT formed water-soluble SP at high concentration. Notably, the viscosity of CD-SS-CPT solution increased significantly accompanied by the

enhancement of concentration. A rod-like fiber was mechanically drawn from the highly viscous aqueous solution (Figure 2e), which was direct evidence for the formation of SP. In contrast, negligible changes in diffusion coefficient and molecular weight were monitored for  $\beta$ -CD $\supset$ CPT as its concentration increased (Figures S26 and S27). These measurements firmly verified that CD-SS-CPT was able to form extended and highly molecular weighted SP in aqueous solution driven by the host-guest interaction between  $\beta$ -CD and CPT.

Upon formation of SP, the solubility of CPT dramatically increased to 1740  $\mu\text{g}$  CPT/mL (Figure 2f), which was 232 times higher than that of the native CPT (7.5  $\mu\text{g}/\text{mL}$ ). In sharp comparison, only a moderate improvement in solubility was detected for  $\beta$ -CD $\supset$ CPT (284  $\mu\text{g}$  CPT/mL), emphasizing the significant role of supramolecular polymerization in increasing the solubility of CPT. The reason was that the host-guest complexation effectively inhibited the crystallinity of CPT by the formation of polypseudorotaxane-type SP. On the other hand, the modification of  $\beta$ -CD and CPT was also favorable to increase their solubility, thus greatly enhancing the solubility of CD-SS-CPT.

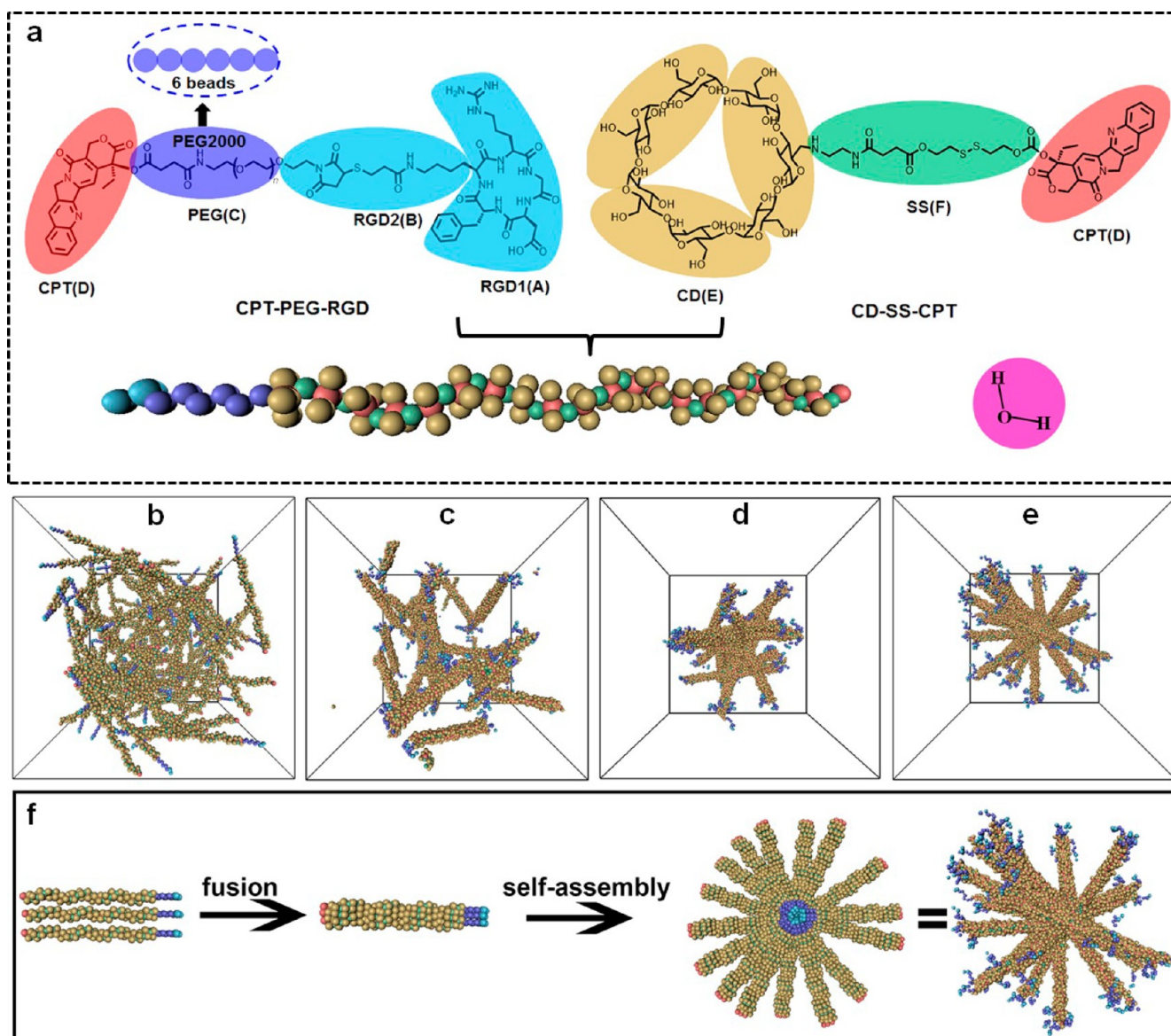


**Figure 4.** (a) Schematic model of water, CPT-PEG-RGD, CD-SS-CPT, and the supramolecular copolymer. (b) The initial snapshot exhibiting randomly distributed SPs in solution. (c) Snapshots showing the formation of many small aggregates, in which intermolecular H-bonds were formed between  $\beta$ -CDs. (d) The snapshot showing SPs joined together and rearrangement. (e) The snapshot showing the final NP structure. (f) The schematic representation of SNPs formation and the corresponding packing model of the building blocks in SNPs.

**Self-Assembly of the Supramolecular Polymer.** For biomedical applications, the size and surface properties of the self-assemblies need to be rationally designed. For SP prepared from CD-SS-CPT, transmission electron microscopy (TEM) indicated that irregular aggregates were formed with the diameter around  $2\ \mu\text{m}$  (Figure 3e), which was unsuitable for intravenous (i.v.) injection. The size of the aggregates needs to be optimized to enhance tumor accumulation of CD-SS-CPT by taking full advantage of the EPR effect. On the other hand, serum protein (opsonin) adsorption of the nanomedicines is another obstacle for clinical use, in which the nanomedicines are greatly uptaken by the reticuloendothelial system (RES) organs and rapidly cleared out from body. Considering these issues, we introduced a polymer (CPT-PEG-RGD) terminated by CPT to construct supramolecular diblock copolymers in situ, where CPT and cRGDFK groups acted as supramolecular initiator and  $\alpha_v\beta_3$  integrin targeting ligand, respectively. PEGylation creates steric hindrance for proteins, remarkably

prolonging the blood circulation and avoiding nonspecific accumulation of the resultant nanostructures. The introduction of cRGDFK ligands on the surface endowed the nanomedicine with excellent targeting capability to specifically deliver CPT to cancer cells overexpressing  $\alpha_v\beta_3$  integrin.

Because of the dynamic nature of noncovalent linkage, the length of the supramolecular segment could be adjusted by controlling the ratio between CD-SS-CPT and CPT-PEG-RGD, possibly optimizing the resultant morphology. TEM study revealed that CPT-PEG-RGD alone self-assembled into micelles in aqueous solution around 15 nm in diameter due to its high hydrophilic/hydrophobic ratio (Figure 3a). The average size was measured to be  $22.6 \pm 3.1\ \text{nm}$  by DLS (Figure 3f), in accordance with the result from TEM study. NPs with diameter ranging from 25–80 nm were formed when the CD-SS-CPT/CPT-PEG-RGD ratio was around 20 (Figure 3b). By increasing the CD-SS-CPT/CPT-PEG-RGD ratio to 40, uniform NPs were obtained with the average diameter of

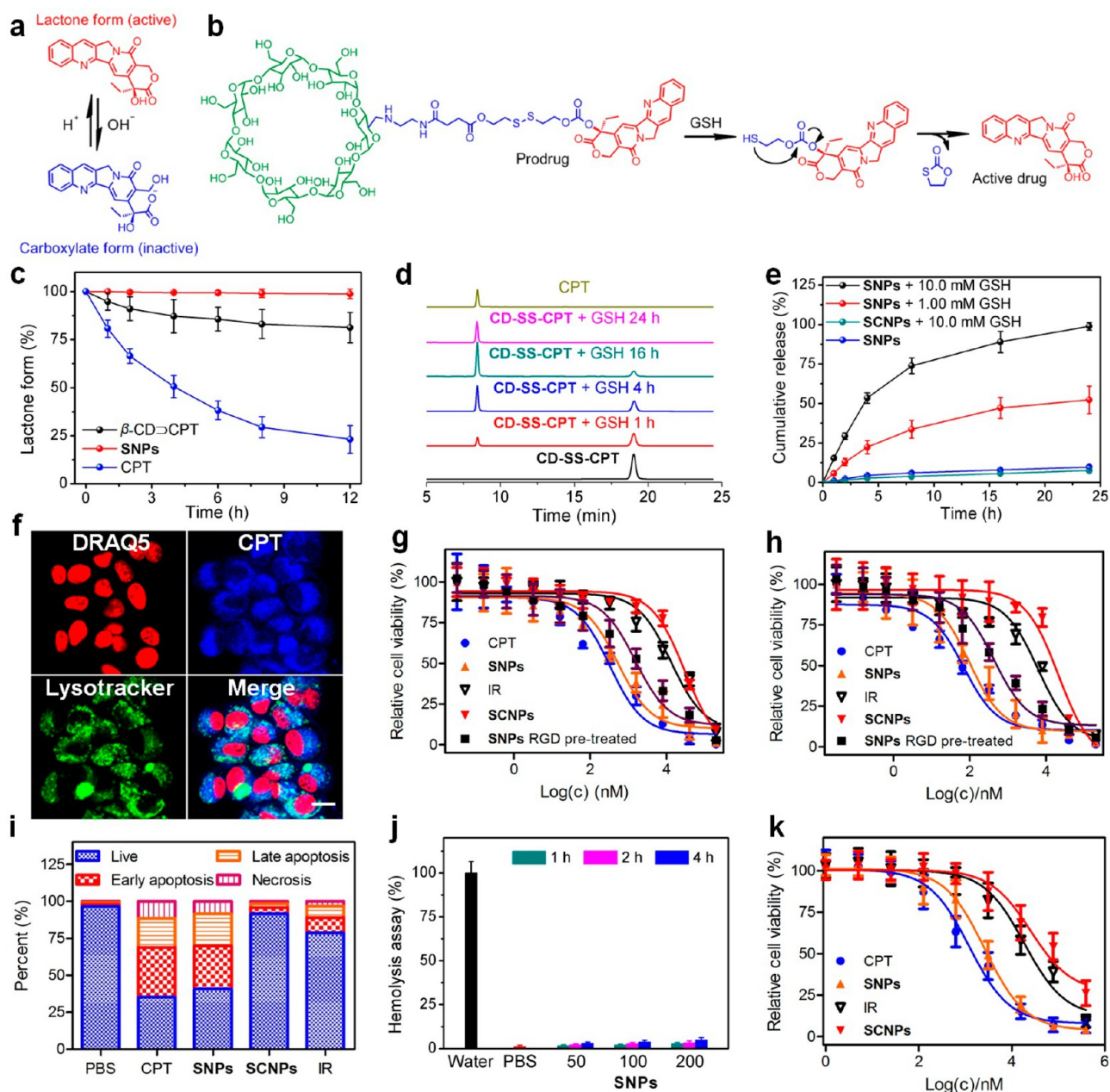


**Figure 5.** (a) The pH-dependent transformation between the lactone form and carboxylate form of CPT. (b) Mechanism of drug release induced by GSH-triggered cascade reaction. (c) Lactone form stability of CPT,  $\beta$ -CD-CPT, and CD-SS-CPT in PBS at pH 7.4. (d) HPLC traces of CD-SS-CPT before and after incubation in PBS containing 10.0 mM GSH for different time. (e) Controlled release profiles of SCNPs and SNPs under different conditions. (f) CLSM images of HeLa cells cultured with SNPs for 8 h. Red fluorescence shows nuclear from DRAQ5; blue fluorescence attributes to CPT; green fluorescence shows lysosomes from lysotracker green. Scale bar is 20  $\mu\text{m}$ . In vitro cytotoxicity of different formulations toward HeLa cells after (g) 24 h and (h) 48 h incubation. (i) Flow-cytometric analysis of Annexin-V/PI dual-staining of HeLa cells after different treatments. The concentration of CPT and IR was 500 nM. (j) Hemolysis rates of SNPs at various concentrations (50, 100, and 200  $\mu\text{g}$  CPT  $\text{mL}^{-1}$ ) after culturing for different time. (k) In vitro cytotoxicity of different formulations toward 4T1 cells after 48 h incubation. Data are expressed as means  $\pm$  s.d.

118 nm (Figure 3c and h). Further enhancement of the CD-SS-CPT/CPT-PEG-RGD ratio to 80 led to the formation of bigger NPs  $\sim$ 150 nm in diameter, while serious aggregation between the NPs occurred (Figure 3d). As a consequence, the average diameter determined by DLS increased to 319 nm (Figure 3i). The reason was that the density of the PEG segments on the surface of the NPs was low, which was hardly to inhibit the internanoparticle interactions through H-bonds between the  $\beta$ -CD.

With these self-assemblies in hand, the stability against dissociation in PBS in the absence or presence of fetal bovine serum (FBS) was evaluated. As shown in Figure 3k, 38.7% of the micelles dissociated after 12 h incubation in PBS. The dissociation rate accelerated remarkably in the presence of 10% FBS, as 92.4% of the micelles disassembled and were released from the dialysis bag. The reason was that the  $\pi$ - $\pi$  stacking interaction was the only driving force for the formation of micelles, which was too weak to stabilize the aggregates in aqueous solution. The sparse PEG corona of the micelles was

unable to effectively inhibit the protein absorption, because the hydrophobic domains in FBS acted as a competitive “host” for CPT driven by hydrophobic interactions, thus greatly speeding their dissociation in the presence of FBS. DLS studies revealed that the average diameter decreased from 22.6 to 15.4 nm by culturing the micelle solution with PBS containing 10% FBS for 24 h (Figure 3f), possibly ascribed to the formation of CPT-PEG-RGD/FBS complex. As compared to the micelles, the stability of the small NPs 67.8 nm in diameter improved little, although a relatively dense PEG shell existed on the surface. As shown in Figure 3g and i, most of the NPs disassembled (90.8%) in the presence of FBS (10%) after 12 h incubation, and only CD-SS-CPT/FBS complex was monitored in DLS measurement with the size of 10 nm after 24 h incubation. The multiple H-bonds between the  $\beta$ -CD and  $\pi$ - $\pi$  stacking interactions between the CPT were responsible for stabilizing the large NPs (319 nm), which could improve their stability to some extent (Figure 3n). However, the sparse PEG chains could not act as an effective protective layer to protect the NPs from being dissociated by FBS. The stability of the nanosheet-like aggregates without PEG corona was poor, which completely dissociated in the presence of FBS within 12 h (Figure 3j and o). Interestingly, SNPs containing dense PEG chains exhibited excellent stability (Figure 3m), where only a small portion disassembled in PBS (9.3%) or even in the presence of FBS (25.2%). The PEG shell on the surface of the NPs acted as surfactant to stabilize the NPs from being dissociated when they were diluted. On the other hand, multiple H-bonds between  $\beta$ -CD, host-guest interactions between  $\beta$ -CD and CPT, and  $\pi$ - $\pi$  stacking interaction between the CPT tails in the core of SNPs provided additional driving forces stabilizing the NPs. Moreover, the dense PEG segments formed “brush-like” superstructures, which prevented FBS from penetrating the surface and circumvented secondary adsorption onto the outer surface of the PEG layer.<sup>31,32</sup> DLS studies showed the average diameter was 91.2 nm after 24 h incubation with 10% FBS solution (Figure 3h), indicating that the structure was greatly maintained, which was extremely important for in vivo applications. Therefore, we chose the NPs of 118 nm in diameter for further in vitro and in vivo investigations because of their relatively high stability, high drug loading content (19.4%), and suitable size falling within the optimal range (10–200 nm) for EPR effect.<sup>33,34</sup>

To better understand the self-assembly mechanism of the supramolecular NPs, dissipative particle dynamics (DPD), a particle-based mesoscaled simulation method, was employed to simulate the self-assembly behavior of the diblock SP in aqueous solution (Figure 4). This method integrates several merits of molecular dynamics, allowing one to simulate the hydrodynamic behaviors of large complex fluid systems up to the microsecond range.<sup>35</sup> One DPD bead represents a group of atoms in this simulation method, and the motions of all beads obey Newton's equations of motion in the system. The components used in this study are comprised of water, RGD, CD, SS, and CPT. Figure 4a shows the simple coarse-grained models of these components. The molecular structure of cRGDfK is separated into two types of beads (RGD1A and RGD2B), and water is represented as a particle “W”. The “C” and “E” beads refer to the PEG segment and  $\beta$ -CD, and the subscript numbers of 6 and 3 refer to the number of the DPD beads. SS and CPT are, respectively, represented by one type of particle. As shown in Figure 4a, a 20 repeat unit model of CD-SS-CPT complexes is constructed. Figure 4b–e exhibits

the snapshots of the self-assembly behaviors in different states using the DPD simulation. After the initially homogeneous state (Figure 4b), the SPs quickly fuse into many small aggregates at  $1 \times 10^4$  DPD time steps driven by the multiple H-bonds between the  $\beta$ -CD (Figure 4c). The aggregates then gradually associate into a large irregular aggregate at  $5 \times 10^5$  DPD time steps (Figure 4d) and finally rearrange into a regular spherical micelle at  $2 \times 10^6$  DPD time steps (Figure 4e). The dynamic formation process of SNPs could be schematically summarized as shown in Figure 4f. There are two stages including “monomers fuse into small aggregates” and “small aggregates associate and rearrange to form spherical SNPs”.

**In Vitro Anticancer Efficacy.** Apart from the enhancement in solubility of CPT, supramolecular polymerization also significantly improved the stability of CPT from hydrolysis in physiological environment. The lactone form of CPT is active for its anticancer behavior, while its carboxylate form is inactive and favored at physiological pH (Figure 5a), thus resulting in a loss of anticancer efficacy.<sup>24</sup> For free CPT, 76.9% of the lactone form was transformed into the carboxylate form within 12 h in PBS buffer at pH = 7.4 (Figure 5c). The hydrolysis rate slowed upon formation of  $\beta$ -CD-CPT, because CPT deeply penetrated into the hydrophobic cavity of  $\beta$ -CD, inhibiting the lactone ring opening. Because of the covalent substitution of CPT on its 20-OH and noncovalent complexation, the lactone form of CPT was greatly maintained. Negligible carboxylate forms of CD-SS-CPT were detected in the same period of time. This observation confirmed that the anticancer efficacy could be effectively preserved by the formation of SP, which was important for in vitro and in vivo anticancer treatments.

To maintain the anticancer efficacy toward cancer cells while reduce its side effect to normal cells, we employed a redox-responsive disulfide bond (–SS–) to connect the host and guest. In the bloodstream, the concentration of GSH is low (1–10  $\mu$ M), and thus CD-SS-CPT is stable and inactive during blood circulation, while this prodrug is activated into highly toxic CPT by the elevated concentration of GSH inside cells (1–10 mM) through a GSH-triggered cascade reaction (Figure 5b).<sup>36</sup> Furthermore, the intracellular GSH level in cancer cells is much higher than that in normal cells, which is further favorable to avoid side effects. High performance liquid chromatography (HPLC) was employed to test the cleavage of the –SS– bond following exposure to GSH. For CD-SS-CPT, a peak at 19.1 min in the HPLC chromatogram was detected (Figure 5d). After incubating CD-SS-CPT with 10.0 mM of GSH for 1 h, a new fragment peak at 8.45 min appeared corresponding to CPT, which became stronger by extending the culture time accompanied by diminishing the peak of CD-SS-CPT. CD-SS-CPT was completely cleaved into CPT and  $\beta$ -CD-SH after 24 h of incubation, demonstrating its excellent GSH-responsiveness.

We monitored the release behaviors of CPT from the SNPs in the absence and presence of GSH using a dialysis method (Figure 5e). In the absence of GSH, SNPs were very stable, as only a small amount of CPT (8.9%) released within 24 h. In sharp comparison, 98.9% of CPT released from the dialysis bag in PBS containing GSH (10.0 mM) over the same experimental period. The release rate was significantly slowed when the concentration of GSH decreased to 1.00 mM, as only 52.3% of free CPT was detected after 24 h incubation, thus verifying that the –SS– bond was readily cleaved by GSH. The TEM image indicated that SNPs dissociated into irregular aggregates upon treatment with GSH for 24 h (Figure S28),

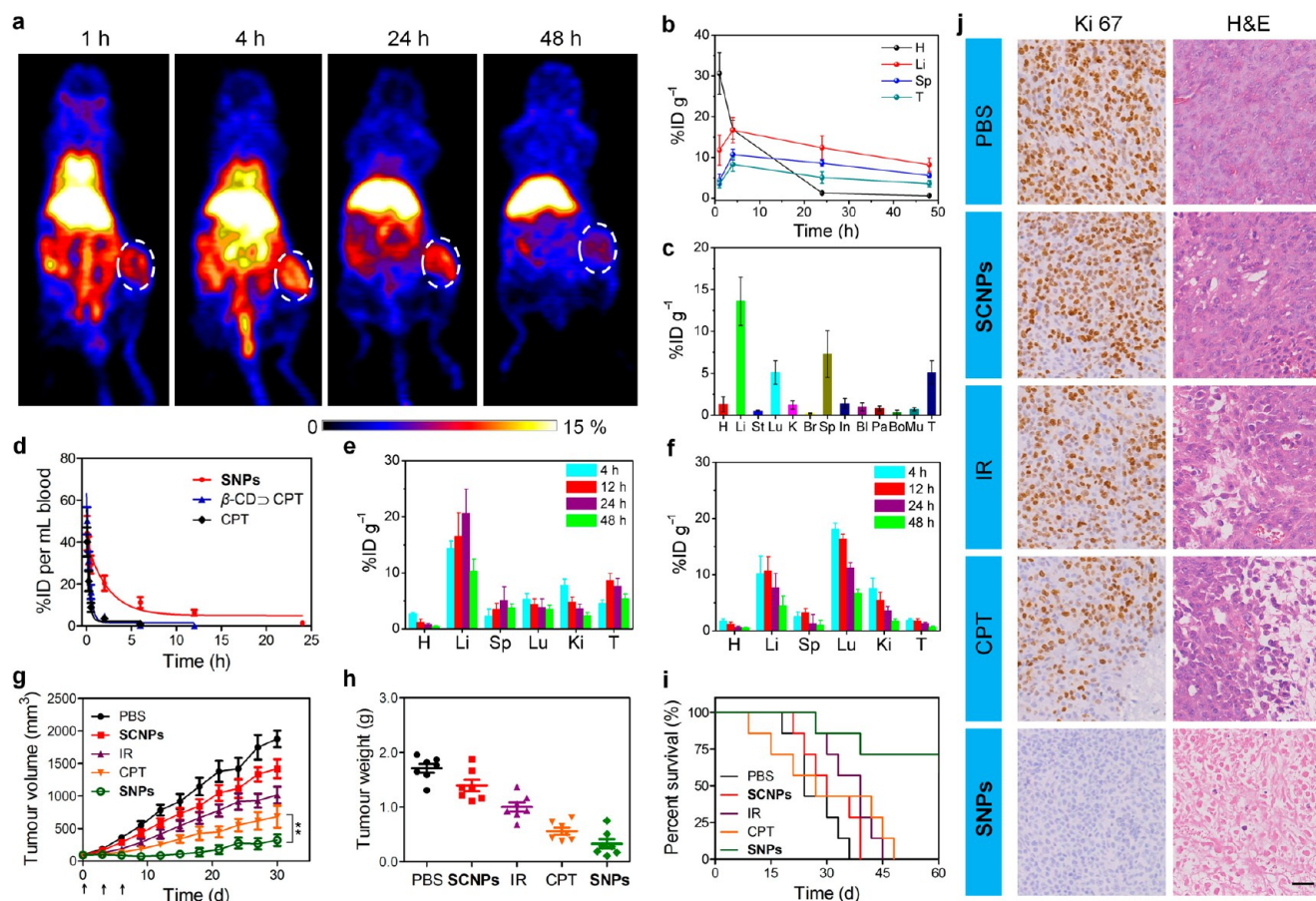


**Figure 6.** (a) Decay-corrected whole-body coronal PET images of HeLa tumor-bearing mice at 1, 4, 24, and 48 h after i.v. injection of  $^{64}\text{Cu}@$ SNPs. The white dashed circles denote the tumor. (b) Time-activity curves quantified on the basis of PET images ( $n = 3$ ). (c) Biodistribution of the  $^{64}\text{Cu}@$ SNPs in mice bearing HeLa tumors at 24 h postinjection ( $n = 3$ ). (d) In vivo pharmacokinetics of free CPT,  $\beta$ -CD-CPT, and SNPs analyzed by HPLC ( $n = 3$ ). (e) Tissue distribution of overall CPT content in the main organs at 24 h postinjection of SNPs. (f) Tissue distribution of CPT in the main organs at 24 h postinjection of free CPT. H, heart; Li, liver; Lu, lung; Sp, spleen; K, kidney; T, tumor. (g) Tumor volume changes of the mice bearing HeLa xenografts treated with different formulations ( $n = 7$ ).  $^{**}p < 0.01$ . (h) Tumor weight and (i) Kaplan–Meier survival curves of the mice bearing HeLa tumors treated with different formulations. (j) H&E and  $\text{Ki}67$  staining of the tumor tissues from each group. Scale bar is 100  $\mu\text{m}$ . Data are expressed as means  $\pm$  s.d.

possibly arising from the precipitation of the released CPT. As a control, negligible release (7.6%) of CPT was measured from the aqueous solution of noncleavable NPs (SCNPs) constructed from CD-CC-CPT and CPT-PEG-RGD even in the presence of high level GSH (10.0 mM). These primary studies demonstrated that SNPs were stable in the bloodstream and extracellular matrix due to the low concentration of GSH, while the immediate release of CPT inside cancer cells was triggered by intracellular GSH.

Confocal laser scanning microscopy (CLSM) and 3-(4',5'-dimethylthiazol-2'-yl)-2,5-diphenyl tetrazolium bromide (MTT) assay were used to assess the targeting ability and anticancer efficacy of the SNPs. Blue fluorescence signal arising from CPT was observed in cytoplasm after culturing the HeLa cells with SNPs for 8 h, indicating that the SNPs were effectively internalized. It should be pointed out that there was an overlap between CPT fluorescence and green fluorescence related to Lyso tracker Green, indicating that the SNPs were transported to lysosomes after internalization, where abundant GSH waited to cleave the  $-\text{SS}-$  bond to activate the anticancer drug. Pretreatment of the HeLa cells with free cRGDfk (20  $\mu\text{M}$ ) for 30 min prior to incubation with the SNPs greatly weakened the intracellular fluorescent intensity

due to the blockage of the  $\alpha_v\beta_3$  integrins on cell membrane (Figure S29), strongly supporting a mechanism wherein the SNPs entered into the cells via receptor-mediated endocytosis.

Inspired by the efficient cellular uptake and GSH-responsive activation, the cytotoxicity of the SNPs was evaluated. After 24 h incubation (Figure 5g), the half maximal inhibitory concentration ( $\text{IC}_{50}$ ) value of SNPs was measured to be  $0.529 \pm 0.068 \mu\text{M}$  on the basis of CPT concentration, which was closed to the  $\text{IC}_{50}$  value of free CPT ( $\text{IC}_{50} = 0.327 \pm 0.043 \mu\text{M}$ ), 25.7-fold lower than that of the FDA-approved anticancer drug Irinotecan (IR) with an  $\text{IC}_{50}$  of  $13.6 \pm 1.64 \mu\text{M}$ , and 58.0-fold lower than that of SCNPs ( $\text{IC}_{50} = 30.7 \pm 4.93 \mu\text{M}$ ). The targeting capability of SNPs was further confirmed by pretreating the HeLa cells with free cRGDfk, in which the  $\text{IC}_{50}$  value increased to  $1.53 \pm 0.27 \mu\text{M}$ . An Annexin V-FITC/propidium iodide (PI) dual-staining assay was further utilized to distinguish the presence of apoptotic cells by flow cytometry. Figure 5i showed a large proportion of the apoptotic (50.6%) and necrotic (8.7%) cells were detected for the HeLa cells treated with SNPs, which was comparable to that of free CPT (Figure 5i). However, SCNPs and IR hardly caused cell apoptosis and necrosis at this concentration. After the culture time was extended to 48 h, the  $\text{IC}_{50}$  values were

calculated to be  $0.098 \pm 0.011$ ,  $0.070 \pm 0.009$ ,  $7.58 \pm 0.87$ , and  $21.2 \pm 3.65 \mu\text{M}$  for SNPs, CPT, IR, and SCNPs, respectively (Figure 5h). As compared to SNPs, the anticancer efficacy of SCNPs was remarkably reduced because the active CPT was hardly released due to the shortage of responsiveness, confirming that the GSH-responsive –SS– bond in CD-SS-CPT was pivotal for optimal intracellular drug release and cytotoxicity.

**In Vivo PET Imaging.** To trace the delivery, accumulation, and excretion of the nanomedicines, diagnostic/imaging ability needs to be introduced. Positron emission tomography (PET) imaging, a radionuclide imaging modality, is playing a pivotal role in preclinical research and noninvasive clinical cancer diagnosis.<sup>37–39</sup> As compared to other imaging methods, such as magnetic resonance imaging (MRI) or single photon emission computed tomography imaging (SPECT), PET imaging is able to provide a highly sensitive, noninvasive, and quantitative readout of its pharmacokinetics and organ/tissue targeting efficiency. The hydrophilic tails (NOTA and cRGDfK) did not affect the supramolecular polymerization and self-assembly behaviors of the resultant SPs; therefore, we used CPT-PEG-NOTA to prepare SNPs for in vivo PET imaging. The NOTA ligands appended on the surface of SNPs are chelators to coordinate  $^{64}\text{Cu}$  radiotracer. As indicated by thin layer chromatography (TLC), the radiolabeling yield was as high as 98% by mixing  $^{64}\text{CuCl}_2$  with SNPs at  $37^\circ\text{C}$  under constant stirring. Radio TLC chromatogram also confirmed that the coordination between  $^{64}\text{Cu}$  and NOTA was highly stable (Figure S30), so  $^{64}\text{Cu@SNPs}$  were suitable for in vivo PET imaging.

$^{64}\text{Cu@SNPs}$  (150  $\mu\text{Ci}$ ) were i.v. injected into HeLa tumor-bearing mice, followed by PET imaging at 1, 4, 24, and 48 h post injection. As shown in the whole-body PET imaging (Figure 6a), the main organs including heart, liver, spleen, and tumor were clearly visualized. The blood concentration of  $^{64}\text{Cu@SCNPs}$  in heart slowly decreased over time due to the blood clearance. Importantly, quantitative region-of-interest (ROI) analysis revealed that the accumulation of  $^{64}\text{Cu@SNPs}$  in the tumor occurred very quickly, which was clearly visible at 1 h ( $3.52 \pm 0.54\%$  ID  $\text{g}^{-1}$ ). The tumor accumulation of  $^{64}\text{Cu@SNPs}$  increased to  $8.31 \pm 1.43\%$  ID  $\text{g}^{-1}$  at 4 h and was maintained at  $5.10 \pm 0.87\%$  ID  $\text{g}^{-1}$  at 24 h postinjection (Figure 6b). Such an efficient tumor homing of  $^{64}\text{Cu@SNPs}$  was attributed to the EPR effect and their active targeting capability. For the liver, an increase in radioactivity signals was first detected from  $11.8 \pm 2.74\%$  ID  $\text{g}^{-1}$  at 2 h to  $16.7 \pm 3.16\%$  ID  $\text{g}^{-1}$  at 4 h postinjection, and then decreased to  $12.4 \pm 2.82\%$  and  $8.26 \pm 1.57\%$  ID  $\text{g}^{-1}$  at 24 and 48 h postinjection, respectively. To verify the accuracy of PET quantification analysis, part of the mice were sacrificed for ex vivo biodistribution studies at 24 h postinjection via  $\gamma$  counting (Figure 6c). The uptake of  $^{64}\text{Cu@SNPs}$  by heart, stomach, lung, kidney, brain, spleen, intestine, bladder, pancreas, bone, and muscle was calculated to be  $1.31 \pm 0.34$ ,  $0.45 \pm 0.07$ ,  $5.15 \pm 0.84$ ,  $1.23 \pm 0.38$ ,  $0.21 \pm 0.04$ ,  $7.27 \pm 1.02$ ,  $1.36 \pm 0.27$ ,  $1.07 \pm 0.22$ ,  $0.82 \pm 0.18$ ,  $0.33 \pm 0.06$ , and  $0.64 \pm 0.08\%$  ID  $\text{g}^{-1}$ , respectively, in good agreement with the biodistribution of CPT determined through HPLC analyses (Figure 6e).

**In Vivo Antitumor Performance.** Prior to evaluating the antitumor efficacy of SNPs, hemolysis assay was conducted to access their in vivo biocompatibility. Figure 5j showed that SNPs did not give rise to apparent hemolysis, as the changes in the hemolysis percentage fell within the negligible range (<5%)

as the concentration increased from 50 to 200  $\mu\text{g CPT mL}^{-1}$ . The effect of nanomedicines on hemolysis mainly depends on the zeta potential of the vehicles. For example, cationic surfaces preferentially bind to negatively charged cell membranes, thus promoting hemolysis. For SNPs, the zeta potential was 3.62 mV (Figure S31), favorable to avoid the interactions with the negatively charged membranes of red blood cells. These results confirmed that SNPs were favorable for in vivo utilization.

To extrapolate their pharmacokinetics, CPT,  $\beta\text{-CD}\supset\text{CPT}$ , SCNPs, and SNPs were i.v. injected into the mice, and blood was collected at various time points post injection (Figure 6d and Figure S32). By quantifying the blood CPT concentration using HPLC, the blood circulation half-life of the SNPs was calculated to be  $1.63 \pm 0.22$  h, 6.8 and 10.2 times those of CPT and  $\beta\text{-CD}\supset\text{CPT}$ , respectively. For SNPs, 6.32% and 1.44% ID  $\text{mL}^{-1}$  remained in the plasma at 24 and 48 h post injection. Additionally, the area under the curve of the SNPs was much greater than those of CPT and  $\beta\text{-CD}\supset\text{CPT}$ , suggesting that the circulation time was greatly elongated through nanoformulation. The free CPT amount in the blood was also detected through HPLC to verify the stability of SNPs during blood circulation. Because of the low GSH level, negligible free CPT in blood was detected post injection of SNPs (Figure S33), possibly minimizing their side effects toward normal tissues. Biodistribution analyses indicated that high tumor accumulation of SNPs was monitored ( $4.65 \pm 0.58$ ,  $8.74 \pm 1.21$ ,  $7.62 \pm 1.35$ , and  $5.48 \pm 0.82\%$  ID  $\text{g}^{-1}$  at 4, 12, 24, and 48 h post injection), much higher than that of free CPT ( $1.83 \pm 0.32$ ,  $1.69 \pm 0.41$ ,  $1.30 \pm 0.22$ , and  $0.65 \pm 0.14\%$  ID  $\text{g}^{-1}$  at 4, 12, 24, and 48 h (Figure 6e and f), which was responsible for their high antitumor performance of SNPs.

Encouraged by the excellent in vitro anticancer activity and high tumor accumulation of SNPs, in vivo antitumor therapy was conducted on nude mice bearing HeLa tumors. When the tumor volume reached around 100  $\text{mm}^3$ , the mice were randomly divided into eight groups and administrated with PBS, IR (5.00  $\text{mg kg}^{-1}$ ), CPT (5.00  $\text{mg kg}^{-1}$ ), SCNPs (5.00  $\text{mg CPT kg}^{-1}$ ), and SNPs (5.00  $\text{mg CPT kg}^{-1}$ ), respectively. As shown in Figure 6g, the average tumor volume in PBS-treated group increased rapidly from 102 to 1876  $\text{mm}^3$  after 30 days. As compared to the PBS control, the mice treated with FDA-approved IR only showed limited antitumor efficacy because of its low anticancer efficacy and fast blood clearance. Although SCNPs can be accumulated in tumor tissue through EPR effect and active targeting, their therapeutic outcome was poor, because the active CPT was hardly released due to the noncleavable linkage. The mice administrated with CPT exhibited enhanced antitumor results, but still unsatisfying, which were caused by nonspecific distribution and fast clearance. Excitingly, SNPs displayed the strongest effect on delaying tumor growth with a tumor inhibition rate of 82.9%, attributed to their excellent GSH-responsiveness and specific tumor accumulation. The median survivals were determined to be 24, 39, 30, and 27 days for the mice in the groups with PBS, IR, CPT, and SCNPs, respectively (Figure 6i). Notably, the Kaplan–Meier survival plots indicated that the SNPs treated group exhibited the longest survival time, mainly attributed to the excellent tumor inhibition.

The tumor weight in each group was measured at the end, which further verified that SNPs were the most effective in suppressing tumor growth (Figure 6h). Hematoxylin and eosin (H&E) and immunohistochemical staining (Ki-67) staining were carried out to gain more insight on pathological changes

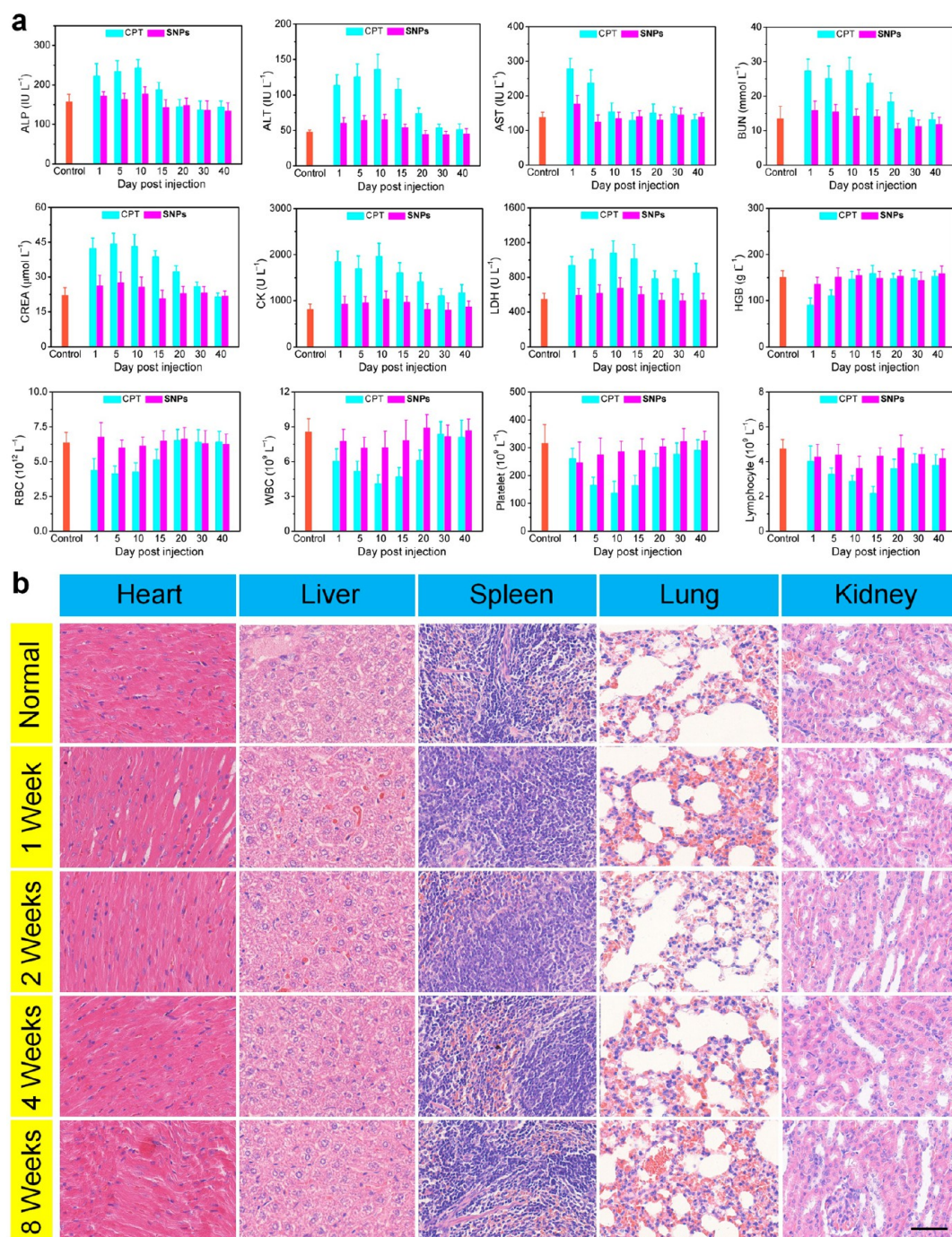


**Figure 7.** (a) Hematology and serum biochemistry test of the mice after treatment with free CPT or SNPs for different time ( $n = 6$ ). (b) H&E staining of the main organ from the mice after treatment with SNPs for different time. Scale bar is 100  $\mu\text{m}$ . Data are expressed as means  $\pm$  s.d.

of the tumors harvested from the mice after different treatments (Figure 6j). The tumor tissues from the mice treated with PBS appeared to be mostly hypercellular and showed an increased extent of nuclear polymorphism. In comparison with the PBS-treated group, varying levels of cell damage were observed for the mice after receiving different administrations, indicating that all of the formulations exhibited antitumor outcomes. Notably, the tumor tissues from the mice treated with SNPs exhibited the highest level of necrosis and the fewest tumor cells, confirming massive remission of proliferative activity.  $K_i$  67 staining also showed that administration of SNPs resulted in much less proliferating

$K_i$  67-positive cells, confirming an enhanced efficacy of SNPs in inhibiting tumor growth.

**Systemic Toxicity and Immunotoxicity Evaluations.** Systemic toxicity of the nanomedicines is an important parameter for preclinical evaluation. Body weight changes and survival time of the mice receiving different treatments always reflect the systematic toxicity. For the mice treated with free CPT, a rapid loss in body weight and a relatively early death were observed after injection (Figure S34), indicating severe side effects occurred caused by the nonspecific distribution of CPT, while the SNPs-treated group displayed negligible body weight fluctuation, even showing a slight

increase from 21.6 to 23.2 g after 30 days. Moreover, no obvious signs of toxic effects, such as eating, drinking, activity, grooming, urination, or neurological status, occurred during the treatment period, which indicated that this supramolecular nanomedicine exhibited low systemic toxicity.

Long-term safety is another important issue before clinical translation of nanomedicines. H&E staining examination was conducted to assess their *in vivo* toxicity (Figure 7b), especially the potential tissue damage, lesions, or inflammation that SNPs may cause. As compared to the healthy mice, no obvious inflammatory lesion and tissue damage were observed in the major organs (heart, liver, spleen, lung, and kidney), further confirming no/very low systemic toxicity of SNPs at our tested dose. Furthermore, no observable accumulation of inflammatory immune cells was detected in the heart, liver, spleen, lung, and kidney, demonstrating that SNPs were safe for *in vivo* practical applications. Alanine aminotransferase (ALT), alkaline phosphatase (ALP), and aspartate aminotransferase (AST) as liver function indicators showed no hepatic dysfunction was induced by SNPs during the therapeutic period (Figure 7a). In addition, no significant differences in renal function indexes were detected between the healthy mice and SNPs treated mice, including blood urea nitrogen (BUN) and creatinine (CREA). Other hematological parameters for the mice administrated with SNPs were all in the normal range, such as creatine kinase (CK), lactate dehydrogenase (LDH), red blood cells (RBC), white blood cells (WBC), hemoglobin (HGB), platelets, and lymphocyte. The reason for their low systemic toxicity was that SNPs were stable during blood circulation where only a small amount of GSH existed, which rarely activated the loaded drug. In sharp comparison, the levels of ALP, AST, ALT, BUN, and CREA were significantly increased for the mice treated with free CPT, indicating the appearances of severe renal toxicity and hepatotoxicity. We also noticed that the level of other markers exceeded the normal range for the mice treated with free CPT during the first days of chemotherapy, convincing evidence for the side effects caused by CPT.

Nanomaterials without apparent *in vitro* and *in vivo* toxicity may still influence various components of the immune systems, thus unintentionally resulting in serious adverse reactions.<sup>40</sup> To guarantee the successful clinic applications of SNPs, their potential effects on immune systems definitely should be carefully assessed. To assess the long-term immunotoxicity of SNPs, we measured the serum levels of a panel of pro- and anti-inflammatory cytokines and chemokines using a multiplex cytokine assay at different time points after *i.v.* injection of high-dose SNPs (10.0 mg CPT kg<sup>-1</sup>). As compared to the normal group, the formulation of SNPs rapidly induced secretions of some pro-inflammatory cytokines at 8 h post injection (Figure 8), such as IL-1 $\beta$ , IL-2, IL-6, IL-17, and TNF- $\alpha$ , because exogenous SNPs caused an inflammatory response. Plasma levels of the T helper 2-related cytokines such as IL-4, IL-9, and IL-13 were not increased. Additionally, other cytokines or chemokines were also upregulated caused by the immune response, such as G-CSF, IFN- $\gamma$ , KC, and MIP-1 $\beta$ . The enhanced expression level of the pro-inflammatory cytokines at 1 day post injection indicated the inflammation still existed. At 4 days post administration, the dysfunctional cytokines and chemokines gradually recovered to normal range, suggesting the inflammatory response weakened benefiting from the rapid clearance of the byproducts. When the experimental time extended to 1 week, almost all of the

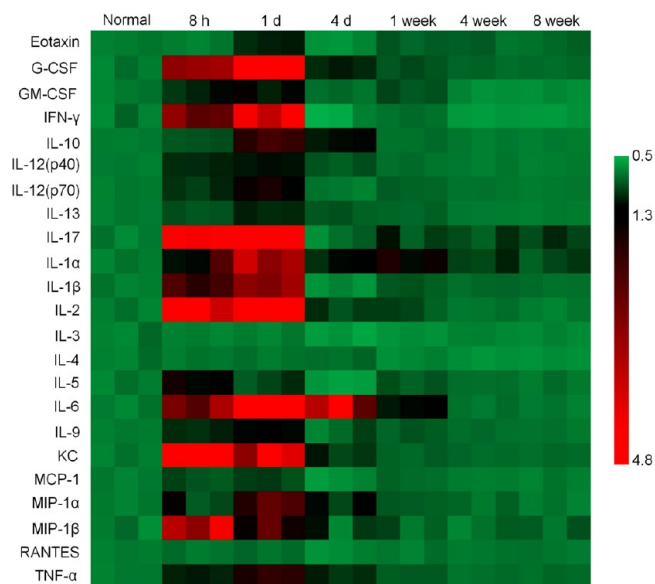


**Figure 8.** Heat map of the relative expression of cytokines and chemokines in serum of C57 mice administrated with SNPs (10.0 mg CPT kg<sup>-1</sup>) at different time post *i.v.* injection ( $n = 3$ ).

cytokines and chemokines returned to normal range. Moreover, negligible immunotoxicity was detected after 4 weeks, confirming our nanomedicine was safe for clinical translation. Unlike the traditional polymers, the backbone of the SPs completely degraded into small molecular weighted components, which could be quickly eliminated from body. Rapid body excretion minimized tissue exposures to the nanomaterials, thus avoiding long-term immunotoxicity.

CD-NOTA was utilized as a model compound with the ability to chelate gallium (Ga) to mimic the clearance behaviors of CD-SH after GSH-triggered cleavage by detecting the Ga amount in the organs at different time post *i.v.* injection using inductively coupled plasma mass spectrometry (Figure S35). It was found that Ga@CD-NOTA was rapidly excreted from body, as evidenced by the quick decrease of Ga level in the main organs within the first 12 h. At 48 h post injection, the Ga content in all measured organs was undetectable including the liver and spleen, which demonstrated the complete clearance of Ga@CD-NOTA. Moreover, the Ga amount in urine and feces was also measured to study the excretion pathway of Ga@CD-NOTA. A high level of Ga was detected in the urine, particularly in the first 4 h, indicating that Ga@CD-NOTA was mainly excreted through renal pathway. From this mimic study, the PET imaging results, and the biodistribution evaluations, we knew that the SNPs were majorly cleared through the liver/spleen (Figure 6a–c and e), while their metabolite was mainly cleared through the kidneys. Such a rapid excretion behavior benefiting from the supramolecular chemistry was rarely observed in traditional polymeric nanomedicines with sizes larger than the kidney filtration threshold. It is thus reasonable to conclude that such supramolecular polymeric nanomedicine with efficient excretion behaviors and absence of acute toxicity is unlikely to induce long-term toxic effects to the treated animals. All of these evaluations demonstrated that this supramolecular nanomedicine could be safely used in cancer treatment.

**Treatment of Orthotopic Breast Cancer and Inhibitory Effects on Lung Metastasis.** Metastasis, the spread of

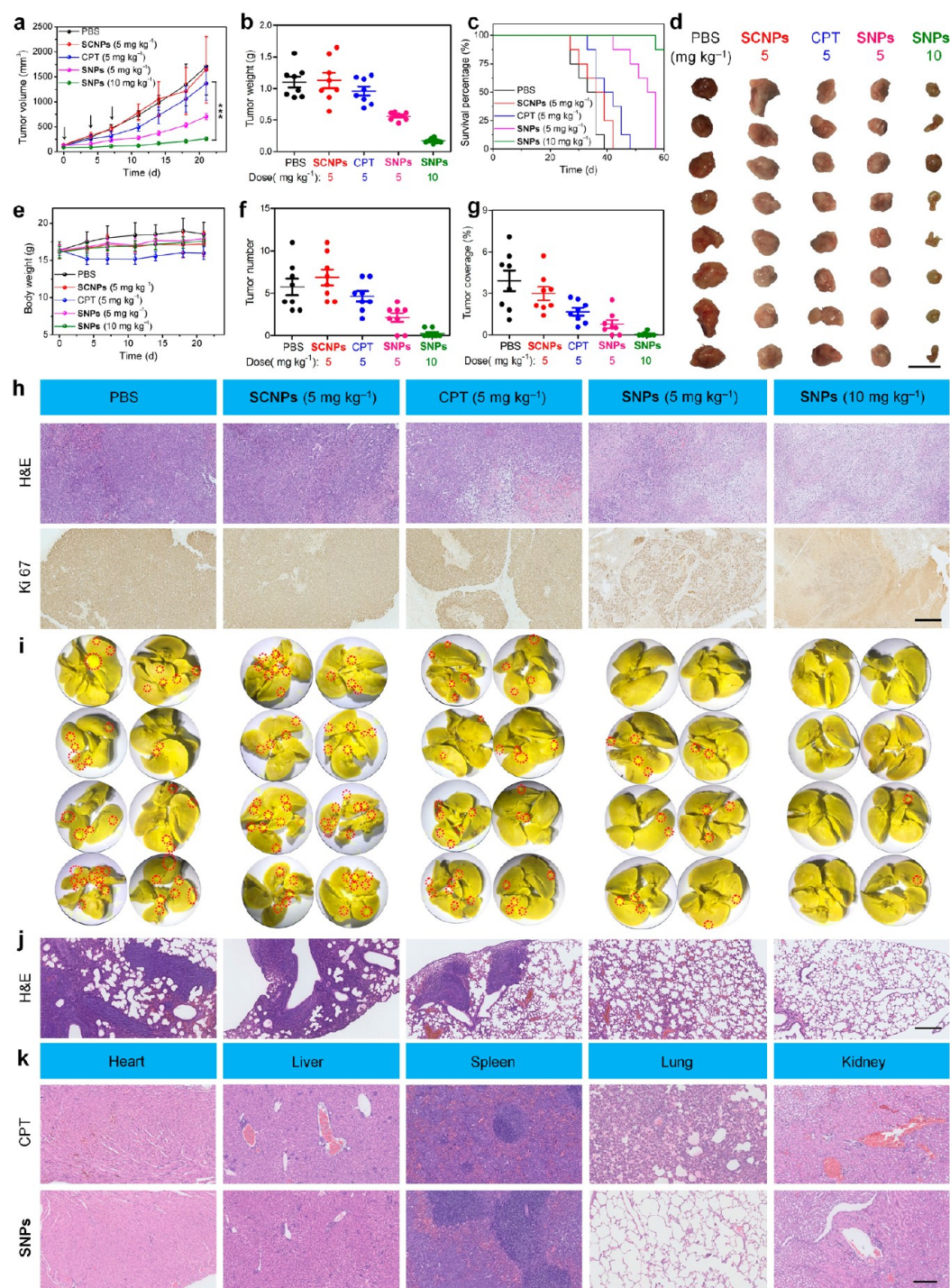


**Figure 9.** (a) Tumor volume changes, (b) tumor weight, and (c) Kaplan–Meier survival curves of the mice bearing orthotopic 4T1 breast tumors treated with different formulations ( $n = 8$ ).  $***p < 0.001$ . (d) Photo images of the orthotopic tumors harvested from the mice after treatment with different formulations. Scale bar is 2 cm. (e) Body weight changes of the mice bearing orthotopic 4T1 breast tumors treated with different formulations. (f) The numbers of tumor nodules present on the lung surface from each group. (g) Tumor coverage percentage in the lungs from each group. (h) H&E and Ki 67 staining of the tumor tissues from the mice treated with different formulations. Scale bar is 2 mm. (i) Photo images of the lungs excised from each group. The red circles denote the visually detected metastatic nodules. (j) Histological examination of metastatic lesions in lung tissues from each group after H&E staining. Scale bar is 1 mm. (k) H&E staining of the main organs from the mice treated with CPT ( $5.00 \text{ mg kg}^{-1}$ ) and SNPs ( $10.0 \text{ mg kg}^{-1}$ ). Scale bar is  $250 \mu\text{m}$ . Data are expressed as means  $\pm$  s.d.

surviving cancer cells from a primary tumor that colonize in distant organs to form secondary tumors, is the greatest contributor to deaths from cancer.<sup>41–43</sup> According to the SEER database from the National Cancer Institute, the 5 year survival rate is only about 20% for stage IV breast cancer,

which makes metastatic breast cancer the second leading cause of cancer related deaths among women.<sup>44–46</sup> Although cancer therapeutic modalities are improving over past years, the therapeutic outcomes are still poor for most chemotherapy patients, and the overall survival is improved by only a few

months at most. The reason is that the injection dose in chemotherapy is unable to fully kill cancer cells in primary tumor sites considering their severe side effects. On the other hand, the anticancer drug can hardly reach the metastatic sites, thus limiting the antimetastasis effect of chemotherapy. Encouraged by the superior antitumor performance and negligible toxicity of SNPs, we anticipated to apply this nanomedicine to treat more aggressive orthotopic breast cancer. From the MTT assay shown in Figure S*k*, the  $IC_{50}$  values of CPT, SNPs, SCNPs, and IR were determined to be  $1.12 \pm 0.17$ ,  $1.89 \pm 0.24$ ,  $25.6 \pm 3.79$ , and  $19.3 \pm 3.57 \mu\text{M}$ , respectively, indicating that SNPs possessed high anticancer activity against 4T1 cell line.

To validate the merit of SNPs on the antimetastasis efficacy, 4T1 tumors were inoculated in the fat pads to establish spontaneous lung metastatic breast cancer, which is a suitable orthotopic model for stage IV human breast cancer. From biodistribution analyses shown in Figure S36, high tumor accumulation of SNPs was observed, and active CPT was able to be released from the nanomedicine triggered by the high intracellular GSH concentration (Figure S37). When the tumor volume reached around  $100 \text{ mm}^3$ , the mice were randomly separated into five groups ( $n = 8$ ) and administrated with PBS, SCNPs, CPT ( $5.00 \text{ mg kg}^{-1}$ ), SNPs ( $5.00 \text{ mg CPT kg}^{-1}$ ), and SNPs ( $10.0 \text{ mg CPT kg}^{-1}$ ), respectively. Considering the low systemic toxicity of SNPs, we increased the injection dose aiming to enhance antitumor efficacy and antimetastasis outcome. For the mice treated with PBS, the tumor volume rapidly increased to  $1708 \text{ mm}^3$  within 21 days (Figure 9a). As compared to the control group, SCNPs did not show any antitumor efficacy, because the active CPT was unable to be released. For the mice administrated with CPT, moderate tumor inhibitions were detected; about 19.6% tumor reduction was achieved as compared to the PBS-treated group. Benefiting from the EPR effect, active targeting ability, and GSH-responsiveness, the formulation of SNPs ( $5.00 \text{ mg CPT kg}^{-1}$ ) resulted in higher antitumor efficacy with a tumor reduction of 58.5%. Excitingly, the antitumor efficacy was remarkably improved by increasing the injection dosage of SNPs to  $10.0 \text{ mg CPT kg}^{-1}$ , as evidenced by the significant suppression of the primary orthotopic tumors (Figures S38–42).

The tumor weight in each group was measured at the end of the treatment, which also indicated that the administration of high-dose SNPs was the most effective in suppressing tumor growth (Figure 9b). The photographs of excised 4T1 tumors from various groups also showed that the tumor size injected with high-dose SNPs was much smaller than those in the other groups, confirming the much enhanced tumor growth inhibition by SNPs over free CPT (Figure 9d). H&E staining revealed that nucleus fragmentation, chromatin condensation, and necrotic cell death along with tissue disorganization were visible in the tumor tissue from the mice administrated with high-dose SNPs, while tumors from the other therapeutic groups were more viable (Figure 9h).  $K_i 67$  staining of the tumor sections further confirmed significantly enhanced necrosis in the group that received high-dose SNPs (Figure 9h), in agreement with the aforementioned antitumor studies.

The survival rate of the 4T1 tumor-bearing mice after different administrations was described in a Kaplan–Meier plots (Figure 9c). The mice in the PBS-treated group all died by 39 days, attributed to the rapid tumor growth and lung metastasis. The median survival time of the mice in SCNPs-

and CPT-treated groups was 37.5 and 40.5 days, respectively, suggesting the limited therapeutic efficacy of these formulations. The therapeutic efficacy was enhanced for the mice treated with SNPs at the same injection dose ( $5.00 \text{ mg CPT kg}^{-1}$ ) with a median survival of 56 days. Excitingly, only one mouse died within the treatment period (60 days) in the group treated with SNPs at high injection dose ( $10.0 \text{ mg CPT kg}^{-1}$ ), demonstrating its overwhelming antitumor performance as well as the extended survival time. More importantly, negligible changes in body weight were observed during the treatment for the high-dose SNPs-treated mice (Figure 9e), attributed to the low systemic toxicity of this supramolecular nanomedicine. As compared to the normal mice, no inflammation and cell apoptosis/necrosis were found in the heart, liver, spleen, lung, and kidney (Figure S43), implying extremely low side effects. In contrast, a significant reduction in body weight was monitored for the mice treated with CPT due to the nonspecific distribution of the toxic drug. Histological analyses revealed the administration of CPT resulted in a severe side effect toward lung tissue, where the elastic fiber network totally disappeared and numerous inflammatory monocytes were visible (Figure 9k). The reason was that the solubility of free CPT was extremely poor, and precipitates were formed immediately after i.v. injection of CPT and stuck in the lung tissues, thus leading to high pulmonary toxicity. Additionally, nephrotoxicity was also detected in the CPT-treated group, mainly ascribed to the renal excretion pathway of this small molecular weight drug.

Furthermore, the antimetastatic activity of these formulations was assessed by counting the metastatic nodules on lung surface, tumor coverage percentage, and subsequent analysis of lung H&E tissue sections. As compared to the PBS-treated group, extensive tumor nodes were detected on the surface of lungs from SCNPs-, and CPT-treated groups, indicating that only slight inhibition of lung metastasis was achieved by these two formulations (Figure 9i and Figures S44–48). It should be noted that the antimetastatic ability of SNPs improved effectively at the same injection dose; only few metastatic nodes were observed after therapy. As shown in Figure 9f, the average number of metastatic nodules on the lung surface was 5.75, 6.88, 4.62, and 2.12 for the mice administrated with PBS, SCNPs, CPT, and SNPs ( $5.00 \text{ mg CPT kg}^{-1}$ ), respectively. Intriguingly, the high-dose SNPs ( $10.0 \text{ mg CPT kg}^{-1}$ ) significantly reduced metastatic nodules: only one tumor nodule was detected on the surface of two lungs. Accordingly, the high-dose SNPs treatment produced a 95.6% inhibition rate on the lung metastasis of breast cancer, which was 18.5-fold higher than that of the free CPT, demonstrating the excellent antimetastatic efficacy of this supramolecular nanomedicine. H&E staining was also employed to detect the metastatic lesions, which were shown as cell clusters with dark stained nuclei. The metastatic foci were evidently detected in the PBS-, SCNPs-, and CPT-treated groups, but were barely visualized in the groups that received SNPs (Figure 9j). The coverage percentages of the metastasis area were calculated to be 3.92%, 2.99%, 1.67%, 0.71%, and 0.06% for the mice treated with PBS, SCNPs, CPT, SNPs ( $5.00 \text{ mg CPT kg}^{-1}$ ), and SNPs ( $10.0 \text{ mg CPT kg}^{-1}$ ), respectively, in good agreement with the results discussed above (Figure 9g). The higher antimetastatic efficacy of SNPs especially at high injection dose was attributed to the specific and effective targeting capability, excellent anticancer efficacy, and low systemic toxicity.

## CONCLUSIONS

In summary, we developed a GSH-responsive AB-type supramolecular monomer CD-SS-CPT, in which the anticancer drug CPT acted as the guest and  $\beta$ -CD as the host. The supramolecular polymerization significantly improved the solubility of CPT by a factor of 232, and effectively inhibited the lactone ring opening of CPT that was favorable to maintain the anticancer activity of CPT. CPT-PEG-NOTA and CPT-PEG-RGD were utilized to fabricate supramolecular diblock copolymer, which orthogonally self-assembled into SNPs, endowing the resultant SNPs with targeting and imaging abilities. Benefiting from  $\pi$ - $\pi$  stacking interactions, host-guest complexations, multiple H-bonds, and PEG shell protections, SNPs with the diameter of 118 nm exhibited excellent stability in physiological environment. Because of the discrepancy in extracellular and intracellular GSH concentration, the premature release of CPT was inhibited during the circulation, while the nanomedicine was activated after being internalized by cells. By fully taking advantage of supramolecular chemistry and nanotechnology, this supramolecular nanomedicine exhibited superior antitumor performance with negligible systemic toxicity and long-term immunotoxicity. More importantly, this supramolecular nanomedicine exhibited outstanding antitumor outcome against orthotopic breast cancer and antimetastasis effect. On account of its unsurpassable advantages in topological structures and tumor micro-environment-responsiveness, this supramolecular polymeric nanomedicine exhibited excellent antitumor efficacy and antimetastasis effect without noticeable systemic toxicity and long-term immunotoxicity, opening a new door to supramolecular polymers for cancer theranostics.

## ASSOCIATED CONTENT

### Supporting Information

The Supporting Information is available free of charge on the ACS Publications website at DOI: 10.1021/jacs.8b04400.

Experimental details, NMR spectra, and other materials (PDF)

## AUTHOR INFORMATION

### Corresponding Authors

\*zwmao@zju.edu.cn

\*chunyangyu@sjtu.edu.cn

\*fhuang@zju.edu.cn

\*shawn.chen@nih.gov

### ORCID

Fuwu Zhang: 0000-0002-1928-3472

Chunyang Yu: 0000-0003-1175-8362

Xinyuan Zhu: 0000-0002-2891-837X

Xiaoyuan Chen: 0000-0002-9622-0870

### Notes

The authors declare no competing financial interest.

## ACKNOWLEDGMENTS

This work was supported by the Intramural Research Program of the National Institute of Biomedical Imaging and Bioengineering, and National Institutes of Health, National Key R&D Program of China (2016YFB0700804), National Natural Science Foundation of China (51673171, 21620102006, 21404070, and 21774077), and Zhejiang Provincial Natural Science Foundation of China (Grant

LR16E030001). The DPD simulations of this work were supported by the Center for High-Performance Computing, Shanghai Jiao Tong University.

## REFERENCES

- (1) Torchilin, V. P. *Nat. Rev. Drug Discovery* **2014**, *13*, 813–827.
- (2) LaVan, D. A.; McGuire, T.; Langer, R. *Nat. Biotechnol.* **2003**, *21*, 1184–1191.
- (3) Petros, R. A.; DeSimone, J. M. *Nat. Rev. Drug Discovery* **2010**, *9*, 615–627.
- (4) Ferrari, M. *Nat. Rev. Cancer* **2005**, *5*, 161–171.
- (5) Peer, D.; Karp, J. M.; Hong, S.; Farokhzad, O. C.; Margalit, R.; Langer, R. *Nat. Nanotechnol.* **2007**, *2*, 751–760.
- (6) Shi, J.; Kantoff, P. W.; Wooster, R.; Farokhzad, O. C. *Nat. Rev. Cancer* **2017**, *17*, 20–37.
- (7) Mura, S.; Nicolas, J.; Couvreur, P. *Nat. Mater.* **2013**, *12*, 991–1003.
- (8) Chen, H.; Zhang, W.; Zhu, G.; Xie, J.; Chen, X. *Nat. Rev. Mater.* **2017**, *2*, 17024.
- (9) Lee, D.-E.; Koo, H.; Sun, I.-C.; Ryu, J. H.; Kim, K.; Kwon, I. C. *Chem. Soc. Rev.* **2012**, *41*, 2656–2672.
- (10) Min, Y.; Caster, J. M.; Eblan, M. J.; Wang, A. Z. *Chem. Rev.* **2015**, *115*, 11147–11190.
- (11) Elsbahy, M.; Wooley, K. L. *Acc. Chem. Res.* **2015**, *48*, 1620–1630.
- (12) Dobrovolskaia, M. A.; Germolec, D. R.; Weaver, J. L. *Nat. Nanotechnol.* **2009**, *4*, 411–414.
- (13) Dobrovolskaia, M. A. *J. Controlled Release* **2015**, *220*, 571–583.
- (14) Brunsveld, L.; Folmer, B. J. B.; Meijer, E. W.; Sijbesma, R. P. *Chem. Rev.* **2001**, *101*, 4071–4098.
- (15) Fang, L.; Olson, M. A.; Benítez, D.; Tkatchouk, E.; Goddard, W. A., III; Stoddart, J. F. *Chem. Soc. Rev.* **2010**, *39*, 17–29.
- (16) Aida, T.; Meijer, E. W.; Stupp, S. I. *Science* **2012**, *335*, 813–817.
- (17) Li, S.-L.; Xiao, T.; Lin, C.; Wang, L. *Chem. Soc. Rev.* **2012**, *41*, 5950–5968.
- (18) Webber, M. J.; Appel, E. A.; Meijer, E. W.; Langer, R. *Nat. Mater.* **2016**, *15*, 13–26.
- (19) Davis, M. E.; Zuckerman, J. E.; Choi, C. H. J.; Seligson, D.; Tolcher, A.; Alabi, C. A.; Yen, Y.; Heidel, J. D.; Ribas, A. *Nature* **2010**, *464*, 1067–1071.
- (20) Namgung, R.; Lee, Y. M.; Kim, J.; Jang, Y.; Lee, B.-H.; Kim, I.-S.; Sokkar, P.; Rhee, Y. M.; Hoffman, A. S.; Kim, W. J. *Nat. Commun.* **2014**, *5*, 3702.
- (21) Clark, A. J.; Wiley, D. T.; Zuckerman, J. E.; Webster, P.; Chao, J.; Lin, J.; Yen, Y.; Davis, M. E. *Proc. Natl. Acad. Sci. U. S. A.* **2016**, *113*, 3850–3854.
- (22) Davis, M. E.; Brewster, M. E. *Nat. Rev. Drug Discovery* **2004**, *3*, 1023–1035.
- (23) Lu, Y.; Hu, Q.; Lin, Y.; Pacardo, D. B.; Wang, C.; Sun, W.; Ligler, F. S.; Dickey, M. D.; Gu, Z. *Nat. Commun.* **2015**, *6*, 10066.
- (24) Cheng, J.; Khin, K. T.; Jensen, G. S.; Liu, A.; Davis, M. E. *Bioconjugate Chem.* **2003**, *14* (2003), 1007–1017.
- (25) Cheetham, A. G.; Zhang, P.; Lin, Y.; Lock, L. L.; Cui, H. *J. Am. Chem. Soc.* **2013**, *135*, 2907–2910.
- (26) Kang, J.; Kumara, V.; Yang, D.; Chowdhury, P. R.; Hohl, R. *Eur. J. Pharm. Sci.* **2002**, *15*, 163–170.
- (27) Schluep, T.; Hwang, J.; Hildebrandt, I. J.; Czernin, J.; Choi, C. H. J.; Alabi, C. A.; Mack, B. C.; Davis, M. E. *Proc. Natl. Acad. Sci. U. S. A.* **2009**, *106*, 11394–11399.
- (28) Yu, G.; Jie, K.; Huang, F. *Chem. Rev.* **2015**, *115*, 7240–7303.
- (29) Miyauchi, M.; Takashima, Y.; Yamaguchi, H.; Harada, A. *J. Am. Chem. Soc.* **2005**, *127*, 2984–2989.
- (30) Tian, Y.-K.; Shi, Y.-G.; Yang, Z.-S.; Wang, F. *Angew. Chem., Int. Ed.* **2014**, *53*, 6090–6094.
- (31) Knop, K.; Hoogenboom, R.; Fischer, D.; Schubert, U. S. *Angew. Chem., Int. Ed.* **2010**, *49*, 6288–6308.
- (32) Hu, X.; Liu, G.; Li, Y.; Wang, X.; Liu, S. *J. Am. Chem. Soc.* **2015**, *137* (2015), 362–368.

- (33) Maeda, H.; Wu, J.; Sawa, T.; Matsumura, Y.; Hori, K. *J. Controlled Release* **2000**, *65*, 271–284.
- (34) Yu, G.; Cook, T. R.; Li, Y.; Yan, X.; Wu, D.; Shao, L.; Shen, J.; Tang, G.; Huang, F.; Chen, X.; Stang, P. J. *Proc. Natl. Acad. Sci. U. S. A.* **2016**, *113*, 13720–13725.
- (35) Liu, Y.; Yu, C.; Jin, H.; Jiang, B.; Zhu, X.; Zhou, Y.; Lu, Z.; Yan, D. *J. Am. Chem. Soc.* **2013**, *135*, 4765–4770.
- (36) Lee, M. H.; Yang, Z.; Lim, C. W.; Lee, Y. H.; Dongbang, S.; Kang, C.; Kim, J. S. *Chem. Rev.* **2013**, *113*, 5071–5109.
- (37) Sun, X.; Cai, W.; Chen, X. *Acc. Chem. Res.* **2015**, *48* (2015), 286–294.
- (38) Heinzmann, K.; Carter, L. M.; Lewis, J. S.; Aboagye, E. O. *Nat. Biomed. Eng.* **2017**, *1*, 697–713.
- (39) Kim, J.; Piao, Y.; Hyeon, T. *Chem. Soc. Rev.* **2009**, *38*, 372–390.
- (40) Elsabahy, M.; Li, A.; Zhang, F.; Sultan, D.; Liu, Y.; Wooley, K. L. *J. Controlled Release* **2013**, *172*, 641–652.
- (41) Schroeder, A.; Heller, D. A.; Winslow, M. M.; Dahlman, J. E.; Pratt, G. W.; Langer, R.; Jacks, T.; Anderson, D. G. *Nat. Rev. Cancer* **2012**, *12*, 39–50.
- (42) Duan, X.; Chan, C.; Guo, N.; Han, W.; Weichselbaum, R. R.; Lin, W. *J. Am. Chem. Soc.* **2016**, *138*, 16686–16695.
- (43) Cao, H.; Dan, Z.; He, X.; Zhang, Z.; Yu, H.; Yin, Q.; Li, Y. *ACS Nano* **2016**, *10*, 7738–7748.
- (44) Steeg, P. S. *Nat. Rev. Cancer* **2016**, *16*, 201–218.
- (45) Eckhardt, B. L.; Francis, P. A.; Parker, B. S.; Anderson, R. L. *Nat. Rev. Drug Discovery* **2012**, *11*, 479–497.
- (46) He, X.; Cao, H.; Wang, H.; Tan, T.; Yu, H.; Zhang, P.; Yin, Q.; Zhang, Z.; Li, Y. *Nano Lett.* **2017**, *17*, 5546–5554.